

1 Evaluation of middle atmosphere temperature and wind 2 measurements and their disturbance characteristics by 3 meteorological rockets

4 Yang He^{1,2}, Jiangping Huang¹, Mingyuan He², Zheng Sheng²

5 ¹Beijing Institute of Aeronautics Meteorology, Beijing 100094, China

6 ²College of Meteorology and Oceanography, National University of Defense Technology, Changsha 410073,
7 China

8 *Correspondence to:* Mingyuan He (hmy008@sina.com) and Zheng Sheng (19994035@sina.com)

9 **Abstract.** It is necessary to carry out the in-situ detection based on the meteorological rocket to deepen the
10 cognitive level of the middle atmosphere environment, though there is still a lack of systematic research on
11 the data accuracy and the physical mechanism affecting the measurement results, which restricts the effective
12 use of rocket data. Based on thermistor and Beidou positioning, combined with temperature correction
13 technology, middle atmosphere temperature and wind measurements from 20-60 km are obtained in
14 northwest China by two meteorological rockets. The detection results are compared with satellite, empirical
15 model and reanalysis data, and the error analysis theory is carried out in combination with the of the drop
16 sounding and atmospheric disturbance characteristics. The results show that the data quality of the rocket
17 detection is ideal, and the variation trend of temperature and wind profile with altitude is consistent with
18 other data. The difference comes from the deviation of the matching data in time and space and the excessive
19 measurement error in the initial fall stage. Also, it is found that the instability of the parachute causes poor
20 positioning data quality and fast falling speed, and eventually cause the measurement error at the
21 corresponding height to be significantly larger. Besides, the profile fluctuation of the first detection is more
22 obvious, which is caused by the fragmentation of the high-altitude gravity wave. Wave dissipation leads to
23 the weakening of atmospheric stability and the generation of denser small-scale layered structures on the
24 profile, making significant wind field changes at the height below through the momentum deposition.

25 1. Introduction

26 The near space is located in the region of 20-100 km, which can cover the stratosphere, the mesosphere
27 and the low thermosphere. The near-space atmosphere is far from the ground and does not have the weather
28 phenomena common in the troposphere (cyclones, thunderstorms, fronts, etc.), but its unique importance still
29 prompts extensive attention and research. First, the near space is the upper boundary of the troposphere,
30 which can be coupled with the troposphere and affect it from top to bottom. The stratospheric atmosphere,
31 due to its slow evolution characteristics (compared with the troposphere), can provide important information
32 for the prediction of extreme weather and climate in the troposphere (Gray et al., 2018; Jin et al., 2023). For
33 example, the weakening of the stratospheric polar vortex is often a precursor to the occurrence of cold waves
34 in the Northern Hemisphere. Second, the near space is the lower boundary atmosphere of space weather,

35 which can act as a "display screen" for solar activity, and the influence of solar activity on Earth's weather
36 and climate can be reflected in it. For example, solar activity can change the ozone in the middle atmosphere
37 and transmit this change to the troposphere through the action of planetary waves (Krivolutsky et al., 2015).
38 In addition, the near space is the combination of aerospace and aviation, and changes in the internal
39 environment will directly affect the flight attitude and effect of aerospace vehicles (Chen et al., 2023; Roney,
40 2007). Atmospheric disturbances, as the superposition of waves at different scales (including turbulence,
41 gravity waves, planetary waves, etc.), are one of the main dynamic processes in the near space. As the height
42 increases, the density decreases exponentially. The amplitude of these disturbances, such as gravity waves,
43 gradually increases during the upward propagating process, and the impact of the wave becomes more and
44 more significant (Lindzen, 1981; Alexander et al., 2010).

45 Since the near space is showing more and more important value, it is urgent to improve the
46 understanding of its internal atmospheric environment. The necessary condition to support this demand is to
47 carry out accurate detection and adequate research. Satellite remote sensing can provide atmospheric profile
48 data with global coverage, but the detection ability of wind field is still insufficient, and the vertical resolution
49 of data is rough (Ern et al., 2022; Thies and Bendix, 2011). Lidar and MST (Meso-Stratosphere-Troposphere)
50 radars can obtain three-dimensional wind fields and temperatures, but the global distribution of detection
51 sites is limited, and the data quality is affected by atmospheric environment and retrieve accuracy (She et al.,
52 2003; Daren et al., 2018; Qiao et al., 2020). Flat-floating balloons with zero pressure or overpressure, can
53 realize continuous detection in the horizontal direction of the stratosphere, but the characteristics of its own
54 drift in the wind bring the uncertainty of detection, and require strict trajectory control technology (He et al.,
55 2024; Alexander et al., 2021). Radiosonde balloons can detect meteorological elements with long time series
56 and high precision, but the highest detection height is generally less than 30 km, and cannot cover higher
57 airspace (He et al., 2022; Yoo et al., 2020). In contrast, the meteorological rocket sounding is the only in-situ
58 detection method that can obtain the atmospheric environment in the altitude range of 20~100 km. The
59 effective evaluation and inspection of rocket detection accuracy is an important prerequisite for the correct
60 use of this means.

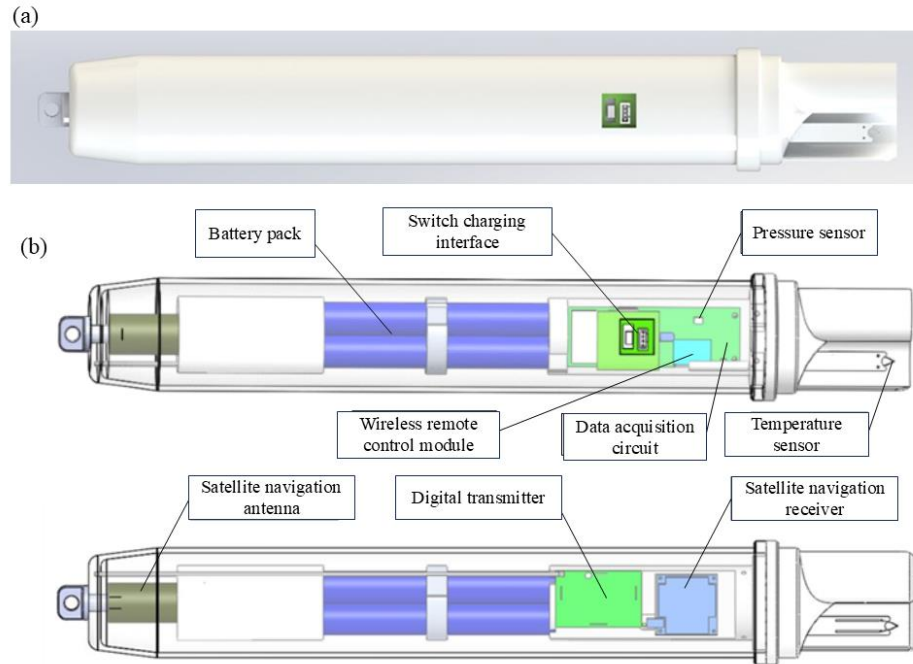
61 The meteorological rocket sounding mainly includes two methods: falling spheres detection and
62 thermistor detection. The falling spheres can obtain the atmospheric density profile of 30-100 km, and then
63 calculate the wind field, temperature and pressure. The thermistor measurement can obtain the atmospheric
64 temperature from 20 to 60 km, and then calculate the density, pressure, and wind field (Eckermann et al.,
65 1995; Wang et al., 2006). Due to the large amplitude of atmospheric waves in this height range, the
66 momentum and energy dissipated by wave fragmentation can cause drastic changes in meteorological
67 elements such as wind field, density and temperature in the surrounding atmosphere. Therefore, analyzing
68 the interaction mechanism between atmospheric wave and background atmosphere has always been one of
69 the important research directions of in-situ observational data. By comparing with satellite, balloon and
70 reanalysis data, thermistor rockets launched from Hainan Station and East China Sea have shown good
71 detection results, and the atmospheric disturbance characteristics in near space are also extracted (Guoying

72 et al., 2011; Song et al., 2024). Atmospheric density is measured using GPS data on a rigid falling ball and
73 the measured deviation from the model results was less than 10% (Yuan et al., 2017). Using passive ball
74 falling experiments in northwest China, in-situ wind field and gravity wave information are analyzed from
75 30 to 100 km (Ge et al., 2019). A comprehensive evaluation of the detection accuracy of the TK-1
76 meteorological rocket is performed and the reliability is demonstrated (Fan et al., 2013). It can be seen that
77 the current results of near space rocket detection are still few, encouraging researchers to work in greater
78 depth.

79
80 In this paper, two meteorological rockets launched in the northwest of China are used to obtain
81 meteorological detection data from 20 to 60 km, error analysis and accuracy evaluation are carried out, and
82 wave disturbance characteristics are also extracted. The structure of the paper is as follows: in the second
83 section, the used data is introduced; in the third section, the temperature correction and error calculation
84 method are given; in the fourth section, the comparison results of rocket detection profile and reference data
85 are discussed, in the fifth section, the error analysis is performed; in the sixth section, the characteristics of
86 wave perturbations and their effects on the background atmosphere are discussed; in the seventh section, the
87 conclusion and prospect are given.

88 **2. Rockets instrument and detection principle**

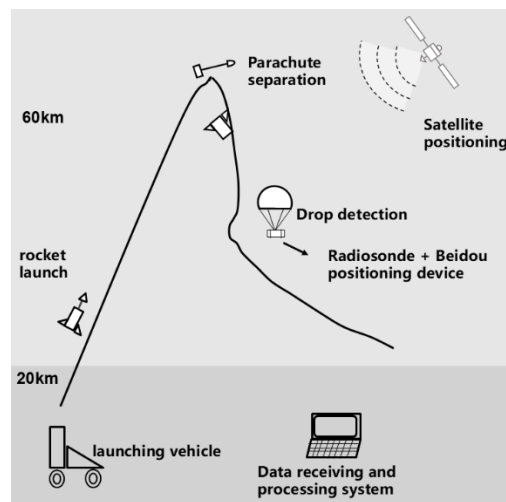
89 The rocket radiosonde is mainly composed of temperature sensors, pressure sensors, satellite navigation
90 and positioning modules, data acquisition circuits, transmitters, wireless remote control modules, batteries,
91 switches, fixed frames, insulation boxes and fiberglass reinforced plastic shells, etc. The temperature sensor
92 adopts a bead thermistor, purchased from the shelf, model MF51MP-D (Blue Crystal Electronics). The
93 pressure sensor adopts a high-precision digital pressure sensor, purchased from the shelf, model ms5607
94 (Switzerland). The navigation and positioning module adopts the high-precision positioning module of
95 Beidou, and the antenna uses a four-arm helical antenna, which is a customized product. The main MCU of
96 the data acquisition circuit adopts a 32-bit processor with ARM core, featuring low power consumption and
97 mixed signal processing capabilities. It has a 14-bit A/D conversion accuracy, which can meet the
98 measurement accuracy requirements of sensors. The digital transmitter is composed of dedicated RF chips
99 and power amplifier modules to form a frequency point digital transmitter. It has the advantages of small size
100 and adjustable frequency. When used in conjunction with ground receiving equipment, it can achieve data
101 transmission within a diagonal distance range of 200 kilometers. The physical appearance and structural
102 layout of the rocket sounding instrument are shown in Figure 1, and the main performance indicators of the
103 rocket sounding instrument are shown in the table A1.



104
105

Figure 1. (a) The physical appearance and (b) structural layout of the rocket sounding instrument.

106 The rocket detection mechanism is shown in Figure 1. The meteorological sonde is carried up by the
 107 rocket, under the action of thrust, it rises at a high speed according to the established trajectory. After the
 108 engine stops working, the rocket uses inertia to continue rising. When the rocket rises near the top of its
 109 trajectory, the parachute carries the sonde and separates from the arrow body. The sonde pulls the parachute
 110 and begins to fall.



111
112

Figure 1. meteorological rocket detection mechanism.

113 During this process, the atmospheric parameters are measured in situ and the data is transmitted down
 114 to the ground receiving system. The thermistor sensor is used to obtain the atmospheric temperature in the
 115 altitude range of 20-60 km, and the atmospheric pressure is obtained layer by layer from iterative calculation

116 based on the base pressure (measured by the pressure sensor at 20 km). Then the atmospheric density is
 117 calculated through the ideal gas equation. The real-time position coordinates (X, Y, Z) of the sonde are
 118 obtained by using the Beidou positioning system, and the first derivative is obtained by linear fitting after the
 119 smoothing position coordinates point by point to calculate the northward, eastward and vertical velocity
 120 (represented by \dot{x} , \dot{y} , and \dot{z}). The corresponding acceleration is obtained by quadratic fitting (represented by
 121 \ddot{x} , \ddot{y} , and \ddot{z}). Based on the velocity and acceleration information, the meridional, zonal, and synthetic wind
 122 are calculated (represented by W_x , W_y , and W), and the wind direction (θ) can be further obtained. The
 123 specific calculation formula is shown in (1)-(4)

$$124 \quad W_x = \dot{x} - \frac{\ddot{x}}{\ddot{z}-g} \dot{z} \quad (1)$$

$$125 \quad W_y = \dot{y} - \frac{\ddot{y}}{\ddot{z}-g} \dot{z} \quad (2)$$

$$126 \quad W = \sqrt{W_x^2 + W_y^2} \quad (3)$$

$$127 \quad \theta = \begin{cases} \arctan \left| \frac{W_y}{W_x} \right| + 180^\circ, (W_x > 0, W_y > 0) \\ -\arctan \left| \frac{W_y}{W_x} \right| + 180^\circ, (W_x > 0, W_y < 0) \\ -\arctan \left| \frac{W_y}{W_x} \right| + 360^\circ, (W_x < 0, W_y > 0) \\ \arctan \left| \frac{W_y}{W_x} \right|, (W_x < 0, W_y < 0) \end{cases} \quad (4)$$

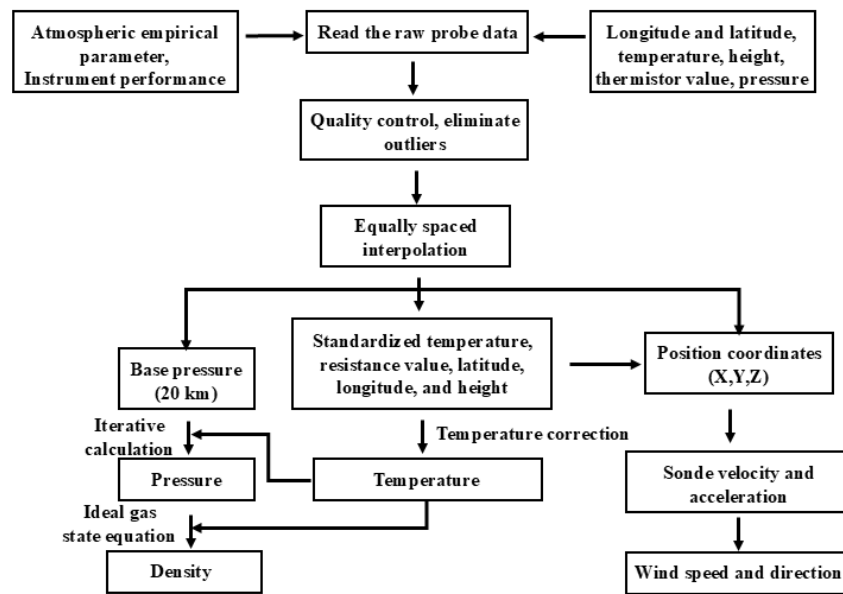
128 The air pressure at each height layer is calculated from the measured base point air pressure (20 km)
 129 using the pressure height formula:

$$130 \quad P = P_d \exp \frac{-g_0(H - H_d)}{R * T_d}$$

131 Among them, P represents the air pressure at the calculated height, P_d is the air pressure of the adjacent
 132 lower layer, H is the geopotential, H_d is the geopotential of the adjacent lower layer, R is the dry air gas
 133 constant, and T_d is the temperature of the adjacent lower layer. Given the temperature and air pressure, the
 134 atmospheric density can be calculated through the ideal gas state equation.

135 The specific calculation process of atmospheric parameters is shown in Figure 2.

136



137

138

Figure 2. Atmospheric parameters calculation process.

139 3. Data introduction

140 The data for the two rockets used in this paper are launched in northwest China in the autumn of 2023,
 141 the vertical profile of wind velocity (synthetic wind, zonal wind, meridional wind), wind direction,
 142 atmospheric temperature, pressure, and density from 20~60 km (effective height interval for analysis) are
 143 obtained.

144 Sounding of the Atmosphere using Broadband Emission Radiometry (SABER) carried on TIMED
 145 satellite, can obtain the vertical profile of atmospheric temperature, pressure, geopotential height, ozone and
 146 other trace gas volume mixture ratio by limb scanning. Here the Level 2A temperature data from Saber
 147 version 2.0 is selected.

148 MERRA2 (Modern Era Retrospective analysis for Research and Applications version 2) data is an
 149 upgraded version of MERRA data, which is the second generation of high-precision data sets. The data has
 150 a time resolution of 6 h and contains 42 pressure layers ranging from 1000 hPa to 0.1 hPa. The data used in
 151 this paper are zonal wind, meridional wind and atmospheric temperature data. The spatial resolution of the
 152 original data was $0.5^{\circ} \times 0.625^{\circ}$.

153 The NRLMSISE-00 atmospheric empirical model covers the altitude interval from the ground to the
 154 thermosphere (0~1000 km), which can provide reference for the environmental state of the relevant missions
 155 in the space industry. The input parameters include the solar and geomagnetic activity index, date, latitude,
 156 longitude, altitude and local time, and the output elements are the temperature and density profile of the
 157 neutral atmosphere.

158 When using reanalysis, empirical model, satellite data to compare with rocket detection results, it is
 159 necessary to match the time and location of data effectively. The verification data close to the time (<5 h)
 160 and within a certain deviation range of latitude (<4°) and longitude (<4°) are selected and interpolated to the
 161 same vertical grid points as the data processed by the rocket.

162 4. Temperature correction and error calculation

163 4.1 Temperature correction

164 During the process of parachute fall, thermistor and the outside atmosphere has been a heat exchange,
 165 in unit time, thermistor internal energy ΔE , self-heating L , convection exchange heat H , radiation exchange
 166 heat Q , viscous exchange heat M , lead conduction heat exchange N have the following relationships (Wagner,
 167 1964):

$$168 \Delta E = L + H + Q + M + N, \quad (5)$$

169 According to the modified formula given by the World Meteorological Organization on the temperature
 170 detection data of the rocket sonde, formula (5) is expanded to (Organization, 2008):

$$171 T_{\infty} = T_f - \frac{rv_f^2}{2c_p} + \frac{m\tau C}{Ah} \frac{dT_f}{dt} - \frac{A_m \rho_m \alpha_s J}{Ah} - \frac{\alpha_t \sigma (A_a T_a^4 + A_b T_b^4 + A_c T_c^4)}{Ah} + \frac{\varepsilon \sigma T_f^4}{h} - \frac{Q_c}{Ah} - \frac{W_f}{Ah} \quad (6)$$

172 Where T_f is the original temperature, T_{∞} is the temperature after correction. The heating term $\frac{rv_f^2}{2c_p}$
 173 reflects the influence of heat exchange between the thermistor and its boundary layer on the temperature
 174 indication value. The temperature hysteresis term $\frac{m\tau C}{Ah} \frac{dT_f}{dt}$ represents the influence of the hysteresis of
 175 thermistor heat exchange on the temperature indication value. The reflected radiation term $\frac{A_m \rho_m \alpha_s J}{Ah}$
 176 represents the influence of the short-wave solar radiation reflected by the ground and clouds to the sonde on
 177 its temperature indication. The long wave radiation term $\frac{\alpha_t \sigma (A_a T_a^4 + A_b T_b^4 + A_c T_c^4)}{Ah}$ represents the influence of
 178 radio frequency radiation and infrared radiation in the environment of the sonde on the temperature indication.
 179 The external radiation term $\frac{\varepsilon \sigma T_f^4}{h}$ represents the influence of the thermal radiation of the sensor to the sonde
 180 on its temperature indication. The structural heat conduction term $\frac{Q_c}{Ah}$ represents the influence on the
 181 thermistor indication due to the thermal conduction of the sonde support to the thermistor. Measuring current
 182 heating term $\frac{W_f}{Ah}$ indicates the amount by which the temperature indication of the resistance changes due to
 183 the heating of the current. The sonde takes shading measures to ignore the direct solar radiation. The
 184 meanings of each item in equation (6) are shown in Table A1.

185 4.2 Error calculation

186 Temperature measurement error is composed of thermistor static calibration error σT_1 , temperature
187 error caused by position error σT_2 , and temperature correction error ΔT_3 (Wagner, 1964, 1961), the
188 calculation formula is as follows:

$$189 \quad \delta T = \sqrt{\sigma T_1^2 + \sigma T_2^2 + \Delta T_3^2}, \quad (7)$$

190 σT_1 and σT_2 are the systematic errors of the instrument, which are fixed values in calculation, ΔT_3 is
191 the residual error after temperature correction (Eq. 6), and the formula is calculated as:

$$192 \quad \Delta T_3 = \Delta(T_\infty - T_f) = \Delta\left(-\frac{rv_f^2}{2c_p}\right) + \Delta\left(\frac{m_T C}{Ah} \frac{dT_f}{dt}\right) + \Delta\left(-\frac{A_s \alpha_s J}{Ah}\right) + \Delta\left(-\frac{A_m \rho_m \alpha_s J}{Ah}\right) +$$

$$193 \quad \Delta\left(-\frac{\alpha_\epsilon \sigma (A_a T_a^4 + A_b T_b^4 + A_c T_c^4)}{Ah}\right) + \Delta\left(\frac{\epsilon \sigma T_f^4}{h}\right) + \Delta\left(-\frac{Q_c}{Ah}\right) + \Delta\left(-\frac{W_f}{Ah}\right), \quad (8)$$

194 Wind speed error is composed of systematic error and random error. Systematic error is written as:

$$195 \quad \begin{cases} \Delta W_x = \Delta \dot{x} - \frac{\dot{z}}{\dot{z}-g} \Delta \ddot{x} - \frac{\ddot{x}}{\dot{z}-g} \Delta \dot{z} + \frac{\dot{x}\ddot{z}}{(\dot{z}-g)^2} \Delta \ddot{z} \\ \Delta W_y = \Delta \dot{y} - \frac{\dot{z}}{\dot{z}-g} \Delta \ddot{y} - \frac{\ddot{y}}{\dot{z}-g} \Delta \dot{z} + \frac{\dot{y}\ddot{z}}{(\dot{z}-g)^2} \Delta \ddot{z} \end{cases} \quad (9)$$

196 Random error is written as:

$$197 \quad \begin{cases} \sigma_{W_x}^2 = \sigma_{\dot{x}}^2 + \left(\frac{\dot{z}}{\dot{z}-g} \sigma_{\ddot{x}}\right)^2 + \left(\frac{\ddot{x}}{\dot{z}-g} \sigma_{\dot{z}}\right)^2 + \left[\frac{\dot{x}\ddot{z}}{(\dot{z}-g)^2} \sigma_{\ddot{z}}\right]^2 \\ \sigma_{W_y}^2 = \sigma_{\dot{y}}^2 + \left(\frac{\dot{z}}{\dot{z}-g} \sigma_{\ddot{y}}\right)^2 + \left(\frac{\ddot{y}}{\dot{z}-g} \sigma_{\dot{z}}\right)^2 + \left[\frac{\dot{y}\ddot{z}}{(\dot{z}-g)^2} \sigma_{\ddot{z}}\right]^2 \end{cases} \quad (10)$$

198 g is the gravity acceleration, $\Delta \dot{x}$, $\Delta \dot{y}$ and $\Delta \dot{z}$ are velocity fitting deviations, $\Delta \ddot{x}$, $\Delta \ddot{y}$, and $\Delta \ddot{z}$ are
199 acceleration fitting deviations, $\sigma_{\dot{x}}$, $\sigma_{\dot{y}}$, and $\sigma_{\dot{z}}$ are speed random errors, $\sigma_{\ddot{x}}$, $\sigma_{\ddot{y}}$, and $\sigma_{\ddot{z}}$ are acceleration
200 random errors.

201 The total error of wind speed and direction is calculated as follows:

$$202 \quad \begin{cases} \delta W_\epsilon = \sqrt{\delta W_{x,\epsilon}^2 + \delta W_{y,\epsilon}^2} \\ \delta G = \frac{180}{\pi} \sqrt{\left(\frac{W_x \cdot \delta W_{y,\epsilon}}{W_x^2 + W_y^2}\right)^2 + \left(\frac{W_y \cdot \delta W_{x,\epsilon}}{W_x^2 + W_y^2}\right)^2} \end{cases} \quad (11)$$

203 Where $\delta W_{x,\epsilon} = \sqrt{\sigma_{W_x}^2 + \Delta W_x^2}$ is the meridional wind synthesis error, and $\delta W_{y,\epsilon} = \sqrt{\sigma_{W_y}^2 + \Delta W_y^2}$ is the
204 zonal wind synthesis error.

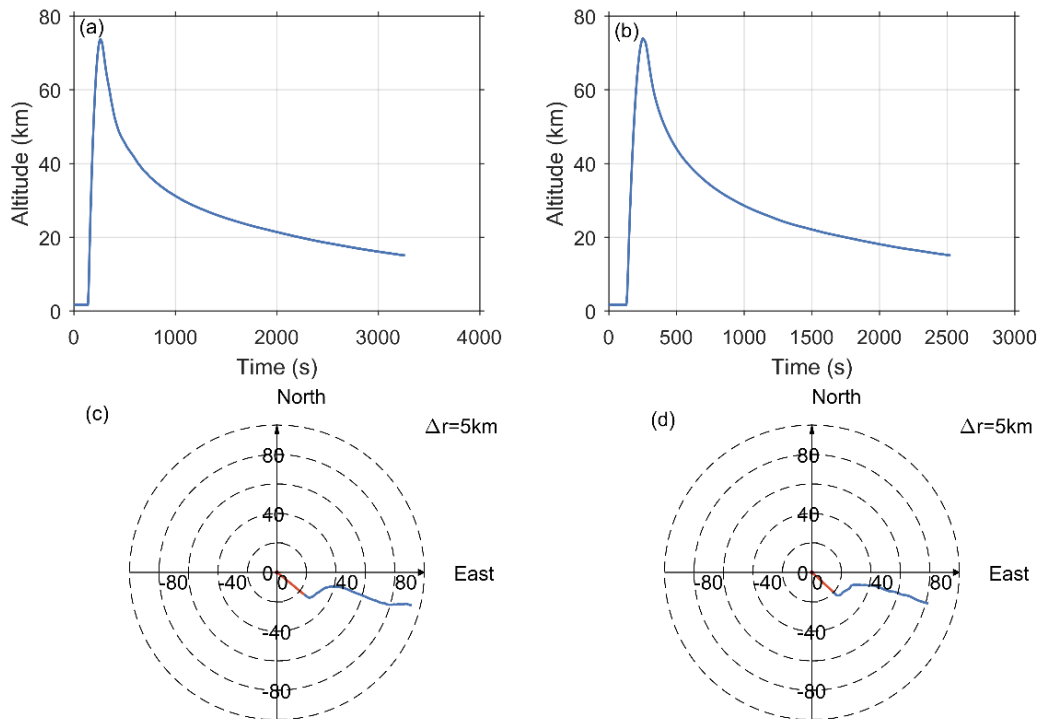
205 5. Comparison of rocket detection results with reference data

206 5.1 Data quality and trajectory analysis

207 The two rockets are referred to as HJ-1 and HJ-2, respectively. HJ-1 is launched at 9:00 UTC on the
208 first day, and HJ-2 is launched at 5:00 UTC on the next day.

209 The time-height curves of HJ-1 and HJ-2 are shown in Figure 3 (top). The actual detection altitude of
210 HJ-1 is about 74 km, the ascent time is about 2 minutes, and the fall time (from the highest point to an altitude
211 of 20 km) is 25 minutes. HJ-2 can reach a maximum altitude of 76 km, the ascent time is about 2 minutes,

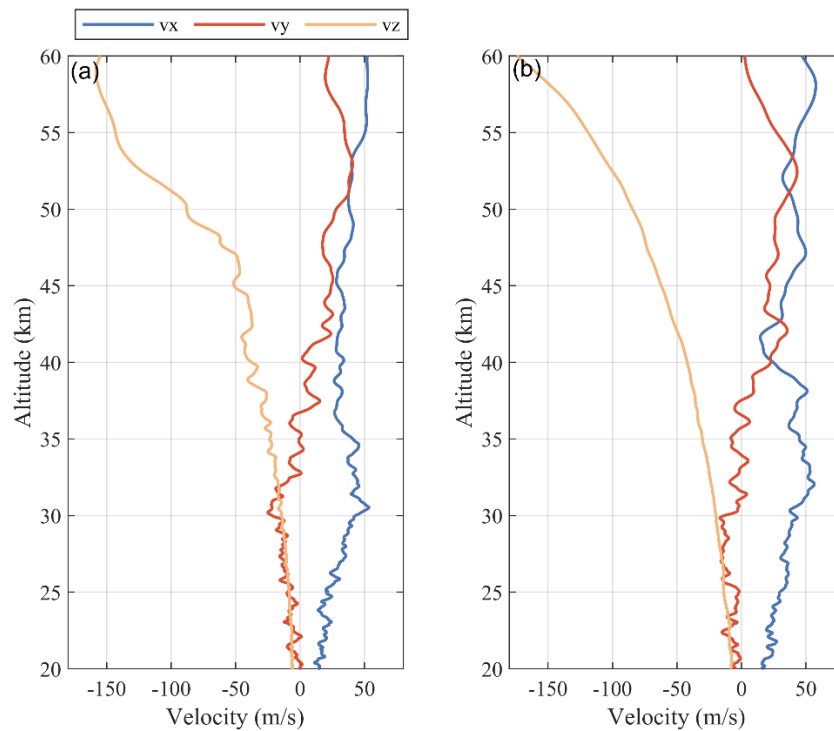
212 and the fall time is 31 minutes. Taking the launch point as the central point, the horizontal motion trajectory
 213 of the ascending stage of rocket launch and the sonde/parachute drift stage are plotted as shown in Figure 3
 214 (below). When the rocket is launched, it rises basically eastward, and after reaching the highest point, the
 215 sonde drifts eastward as it falls with the parachute, which is determined by the background wind field over
 216 the area (the trajectory indicates that the entire layer is dominated by westerly winds). The sonde remained
 217 within 100 km from the launch point during the entire detection process (from the beginning of the launch to
 218 the 20 km falling height).



219

220 **Figure 3. Time-altitude curves of (a) HJ-1 and (b) HJ-2, and horizontal motion trajectory of (a) HJ-1 and (b) HJ-**
 221 **2 (red for rocket ascent, blue for sonde/parachute drift).**

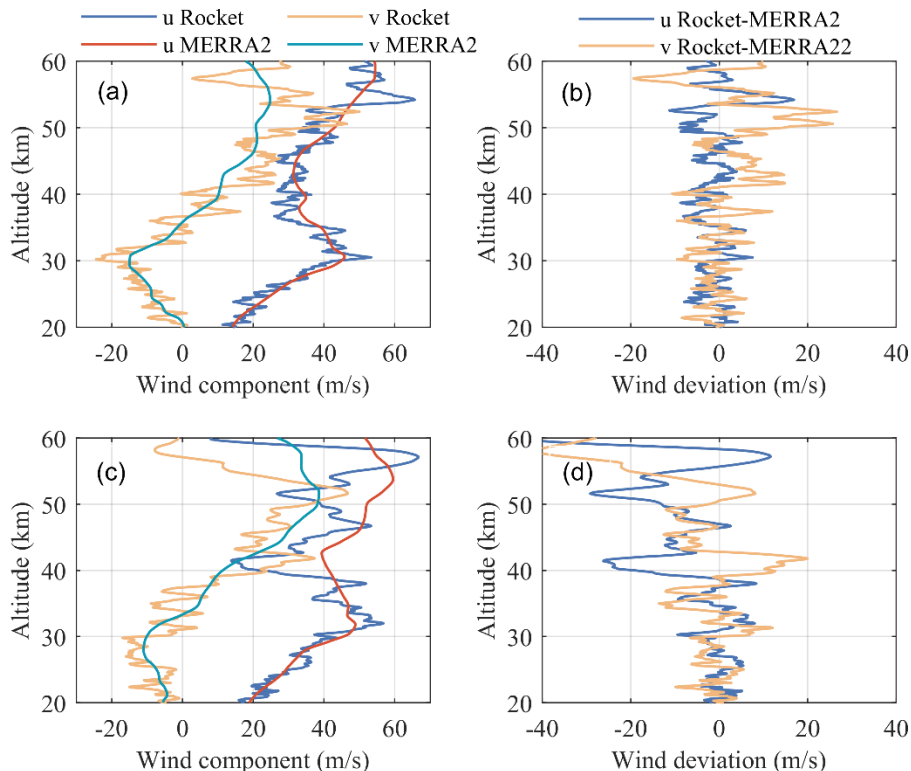
222 In order to further analyze the trajectory characteristics of the sonde during its fall, the vertical
 223 distribution of zonal velocity (v_x), meridional velocity (v_y) and vertical velocity (v_z) are shown in Figure 4.
 224 The zonal velocity of the two rockets is positive, and the meridional velocity gradually changes from positive
 225 to negative, which corresponds to the characteristics of the falling trajectory drifting first to the northeast and
 226 then to the southeast in Figure 3. It is worth noting that there is an obvious disturbance characteristic (denser
 227 small scale layered structure) of vertical velocity for HJ-1, compared with that of HJ-2. After the same data
 228 processing method, the obvious difference of v_z profile roughness may reflect the great difference of
 229 disturbance in the vertical direction at high altitudes.



230
231 **Figure 4. Velocity-altitude curves of (a) HJ-1 and (b) HJ-2.**

232 5.2 Wind and temperature measurements

233 Figure 5 shows the comparison of the zonal and meridional winds obtained by the two rockets with the
 234 MERRA2 data. Before the launch of the rocket, the balloon sounding is also carried out. In the detection
 235 altitude range of the balloon, the wind speed and direction from the rocket are in good agreement with the
 236 balloon profile, and the details of the disturbance are basically consistent (Figure A1), indicating the
 237 reliability of the retrieved wind field results. The meridional winds of the two rockets both reach the
 238 maximum value near 50 km, exceeding 40 m/s. As reflected in Figure 3, in the initial stage of fall after the
 239 rocket body-parachute separation, the trajectory turns from south to north, which proves that the strong
 240 meridional winds dominate at high altitudes.



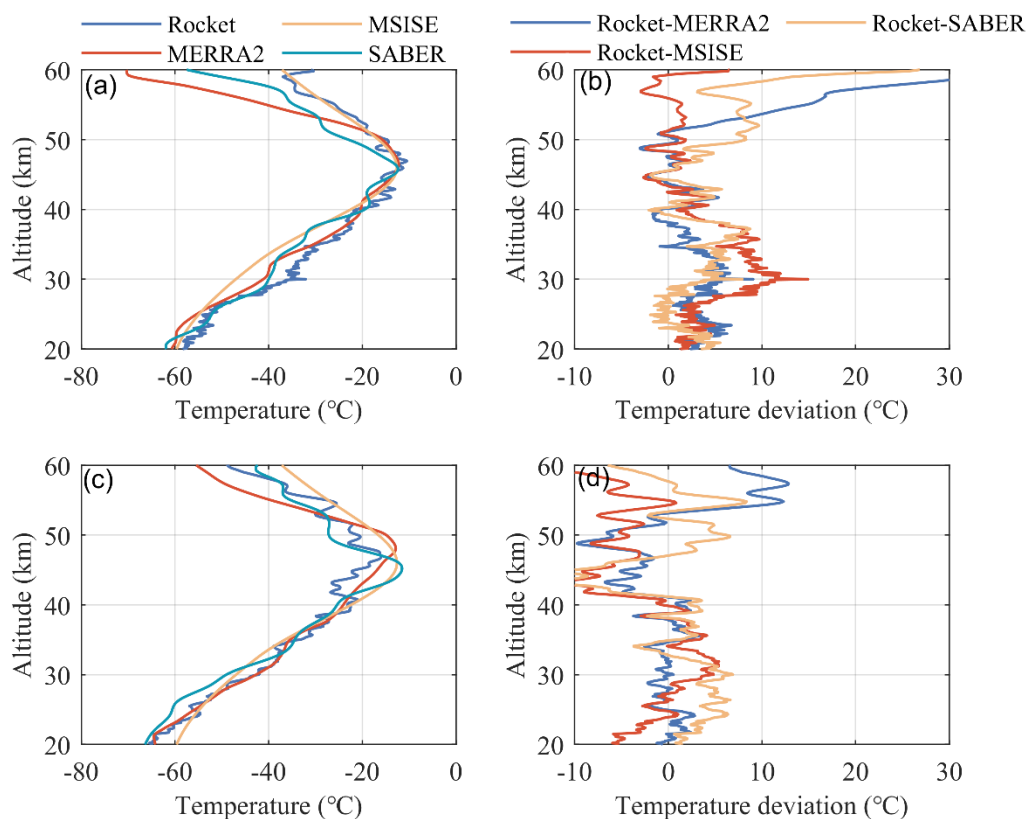
241
242
243
244

Figure 5. (a) The vertical distribution of zonal wind and meridional wind of HJ-1, (b) the difference of HJ-1 velocity component with MERRA2, (c) the vertical distribution of zonal wind and meridional wind of HJ-2, and (d) the difference of HJ-2 velocity component with MERRA2.

245
246
247
248
249
250
251
252
253
254
255
256
257
258
259
260
261

Here, we use the deviation result describes the gap between the rocket detection data and the reference value (satellite, reanalysis, etc.). The purpose is to demonstrate the degree of consistency or deviation between the rocket detection results and other data, and it is a comparison between different data. HJ-1 and MERRA2 have basically the same variation trend of wind speed components at the altitude of 20~60 km, and the zonal wind deviation is relatively small in the whole altitude, while the meridional wind deviation has large positive and negative fluctuations between 50~60 km. The average deviation (absolute value) of the zonal wind at the whole altitude is 3.3 m/s, and that of the meridional wind is 5.4 m/s. In contrast, the measured wind of HJ-2 has greater fluctuation than that of MERRA2, and the deviation between the two increases significantly above 40 km. The average deviation of zonal wind is 7.5 m/s and that of meridional wind is 7.6 m/s. In the altitude range of 20~45 km, the variation trend of wind speed is consistent. At higher altitudes, the measured wind speed of the rocket can show more significant fluctuation characteristics. There are maximum wind speed areas near 30 km and 55 km for both the two rockets, and the maximum near 55 km is difficult to reflect in the MERRA2 data. This indicates that the reanalysis data may lack observation results for assimilation at higher altitudes, and the difference of wind field in the upper stratosphere is obviously greater than that in the lower stratosphere even in the close spatiotemporal range. Considering that the output from the model tends to reflect the average trend, and the transient results of a single detection are more prominent, it is reasonable to have differences between the rocket detection and the model.

262 Figure 6 shows the vertical distribution of temperature from rocket, SABER, MSISE, and MERRA2
 263 data and the corresponding deviation from them. Results before and after temperature correction and
 264 corresponding sub-term correction amount are shown in Figure A2, the temperature correction is larger above
 265 50 km, and gradually decreases below 50 km. Among the various correction sub-items for rocket detection
 266 temperature, the influence degree of pneumatic heating, current heating, and temperature hysteresis are
 267 relatively large, and these influences gradually decrease as the height decreases overall. The corrected
 268 temperature is smaller than original temperature in the entire height. According to the maximum temperature,
 269 the stratopause height measured by the rocket (the height of the inflection point) is around 47 km. The
 270 stratopause height is consistent with other reference data for HJ-1, but shows some differences for HJ-2. The
 271 temperature profiles of the four data have a consistent trend from 20 km to 50 km, with small deviation. The
 272 deviation between the reference data and the rocket detection results increases above 50 km. In this interval,
 273 the temperature deviation between HJ-1 and MISIS is the smallest, while the difference between HJ-2 and
 274 SABER is the smallest. It is worth noting that the temperature deviation of HJ-1 above 57 km has a sharp
 275 trend, which may be resulted from its measurement error (discussed later). The difference of data comparison
 276 may be due to the following reasons: 1) There are deviations in the position and time of the reference data
 277 matching with the rocket; 2) The results of the model reflect the average over time and space, which is indeed
 278 different from the single-point profile.



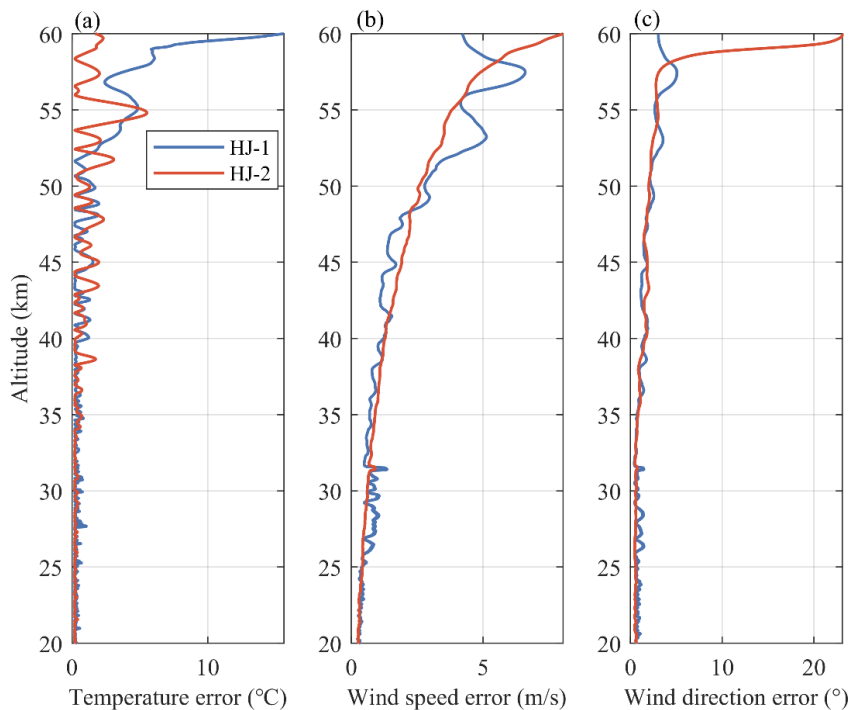
279
 280
 281
 282

Figure 6. (a) The vertical distribution of temperature for HJ-1, (b) the difference of HJ-1 temperature with MERRA2, MSISE, and SABER, (c) the vertical distribution of temperature for HJ-2, and (d) the difference of HJ-2 temperature with MERRA2, MSISE, and SABER.

283 The vertical distribution of rocket detection density and their relative deviations with MERRA2, MSISE,
284 and SABER are also shown in Figure A3. The density relative deviation of HJ-1 shows a significant
285 maximum value between 40 and 50 km (the deviation can reach about 10% for the above three reference
286 data), while the relative density deviation of HJ-2 is significantly smaller, especially with excellent
287 consistency with the SBAER data (the relative deviation within the entire detection height range is within
288 5%). The large density deviation of HJ-1 in the upper atmosphere is, on the one hand, due to the significant
289 reduction in the density itself, which makes the difference more prominent. On the other hand, it is very likely
290 that there are other strong atmospheric disturbances causing drastic changes in density (discussed later),
291 which have not been captured by the model and satellite data.

292 6. Error analysis

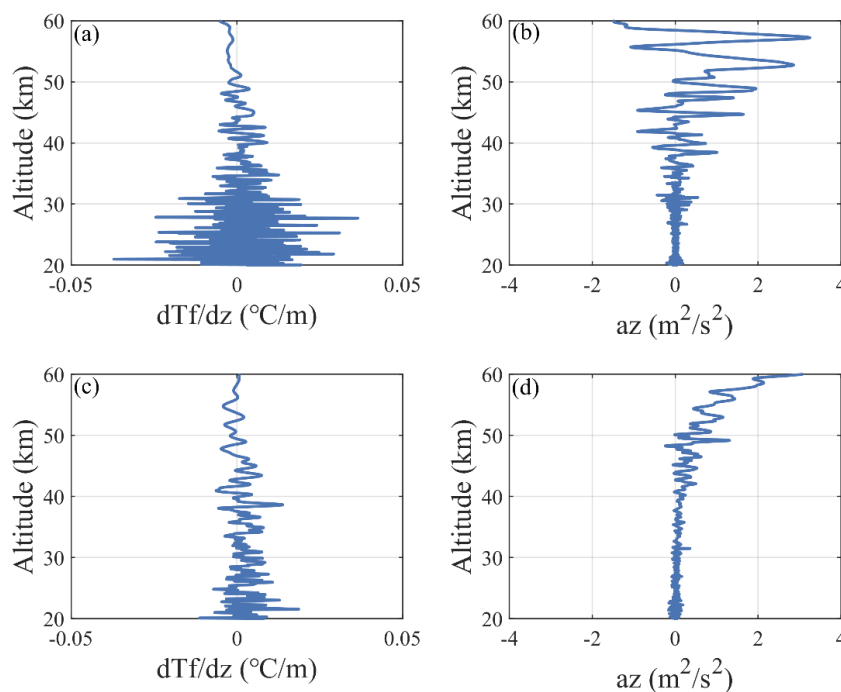
293 Accurate measurement is the prerequisite for conducting further data analysis and application. To further
294 analyze the sources of deviation between the rocket detection results and other data, as well as the reliability
295 of the disturbance analysis, the error level of the rocket instrument is discussed here, [which is a comparison](#)
296 among different heights and sub-items within the rocket own detection results. Temperature and wind
297 measurement errors of HJ-1 and HJ-2 can be obtained according to Eq. 8 and Eq. 11, as shown in Figure 7.
298 Systematic and random errors of wind speeds are shown in Figure A3 and Figure A4, respectively. The
299 atmospheric temperature error level (regional average) of HJ-1 is 0.31 °C, 0.53 °C and 5.5 °C at 20-30 km,
300 30-50 km and above 50 km, while that of HJ-2 is 0.24 °C, 0.55 °C and 1.75 °C. The wind speed error level
301 of HJ-1 is 0.63 m/s, 1.12 m/s and 4.95 m/s at 20-30 km, 30-50 km and above 50 km, while that of HJ-2 is
302 0.38 m/s, 1.19 m/s and 4.0 m/s. The wind direction error levels of HJ-1 are 0.81°, 1.08° and 3.15° at 20-30
303 km, 30-50 km and above 50 km, respectively, while that of HJ-2 is 0.54°, 1.11° and 4.25°. According to Eq.
304 9 and Eq. 10, when the vertical acceleration and vertical velocity are too large, the denominator $\ddot{z} - g$
305 decreases and the numerator \dot{z} increases, which can obviously affect the results of systematic error and
306 random error. In the whole detection section, the same smooth fitting points are used, so the velocity error is
307 consistent. However, due to the large jump of the positioning data, the acceleration ratio in the inertial
308 velocity will also jump. When the falling velocity is large, the product will also increase, resulting in a
309 significantly larger error margin at the high altitudes.



310

311 **Figure 7. Error-height curves of (a) temperature, (b) wind speed, and (c) wind direction for HJ-1 and HJ-2.**

312 The original temperature vertical gradient and vertical acceleration of HJ-1 and HJ-2 are shown in
 313 Figure 8. In the initial falling stage (50-60 km) after the parachute separation, the falling speed is too large,
 314 and the acceleration fluctuates significantly in this height range. The vertical acceleration of HJ-1 has two
 315 peaks between 50-60 km, and there are also maximum values in the corresponding height of the wind speed
 316 random error and systematic error profile (Fig. A3). The vertical acceleration of HJ-2 increases rapidly above
 317 50 km, which also corresponds to the increasing trend of wind speed component in systematic error and
 318 random error. According to the error equation, the measurement error of wind speed depends largely on the
 319 velocity error and acceleration error. At the same time, the temperature error is also related to the vertical
 320 gradient of the measured temperature indication value (in HJ-1, the obvious gradient deviation above 58 km
 321 and its ratio to the convective heat exchange coefficient cause the temperature error to increase sharply),
 322 which is also the reason why the temperature error and wind field error in Figure 7 have inconsistent trends.
 323 Through the above analysis, we believe that the intensity of vertical acceleration fluctuation directly affects
 324 the error results of wind field measurement. At high altitudes (near to 60 km), the parachute swing is large,
 325 and the data reception is not stable, resulting in the relatively low positioning data quality and the large
 326 position error, which finally lead to the relatively large wind field error. As the detection height gradually
 327 decreases, the positioning data quality increases and the measurement error decreases gradually as the
 328 parachute falls steadily.



329
330
331

Figure 8. (a) Temperature gradient-height curve and (b) vertical velocity-altitude curve for HJ-1, (c) Temperature gradient-height curve and (d) vertical velocity-altitude curve for HJ-2.

332 7. Disturbance characteristic analysis

333 In the accuracy analysis of the two rocket detection results, we find that compared with HJ-2, HJ-1 has
334 a more intense falling velocity disturbance, and the deviation from the reference data is larger. Profile
335 deviation phenomena discovered in the result above are inferred to be closely related to the strong disturbance
336 at this height. Therefore, it is necessary to further verify these phenomena in the atmosphere through
337 disturbance characteristic analysis. Conducting wave disturbance analysis here, on the one hand, verify the
338 previous detection results, and on the other hand, it is also an application study of rocket detection data,
339 enhancing the theoretical nature and completeness of the rocket data analysis results.

340 7.1 Wave energy and background field analysis

341 Due to the lack of measured wind field data at high altitudes (30-60 km), the fine structure cognition of
342 wind disturbance at corresponding interval is not sufficient. Many of the sharp peaks in the wind profile
343 captured by balloon and rocket detections are real perturbations in the atmosphere (Figure 5 and Figure A1),
344 which are smoothed out in the reanalysis. In other words, using rocket data may be more suitable for
345 analyzing wave disturbance characteristics at high altitude, since reanalysis data failed to capture these details.
346 The apparent differences in vertical velocity and acceleration of the sonde during its fall (Figure 8) also
347 indicate significant differences in upper atmospheric disturbances. By analyzing the atmospheric background

348 state and gravity wave (GW) information, we compare the difference characteristics of atmospheric
 349 disturbance in two detection processes.

350 GWs are generated by the excitation source at the lower atmosphere, and their amplitudes increase
 351 gradually as the atmospheric density decreases during upward propagation. Wind shear is an important
 352 disturbance source of high-altitude GWs, which can cause GWs to be generated or broken (Larsen, 2002;
 353 Larsen and Fesen, 2009). Vertical wind shear can be calculated by the following formula:

$$354 \quad \frac{dU}{dz} = \sqrt{\left(\frac{du}{dz}\right)^2 + \left(\frac{dv}{dz}\right)^2}, \quad (12)$$

355 Buoyancy frequency N can reflect the unstable state of the atmosphere. $N^2 > 0$ is the static stable state,
 356 and $N^2 < 0$ is the static unstable state. The square buoyancy frequency can be calculated by the following
 357 formula:

$$358 \quad N^2 = \frac{g}{T} \left[\left(\frac{dT}{dz} \right) + \frac{g}{c_p} \right], \quad (13)$$

359 The gradient Richardson number R_i can reflect the ratio of buoyancy work term to shear stress work
 360 term, which can be obtained by the ratio of the square of buoyancy frequency to the square of wind shear:

$$361 \quad R_i = \frac{N^2}{\left(\frac{du}{dz}\right)^2 + \left(\frac{dv}{dz}\right)^2}, \quad (14)$$

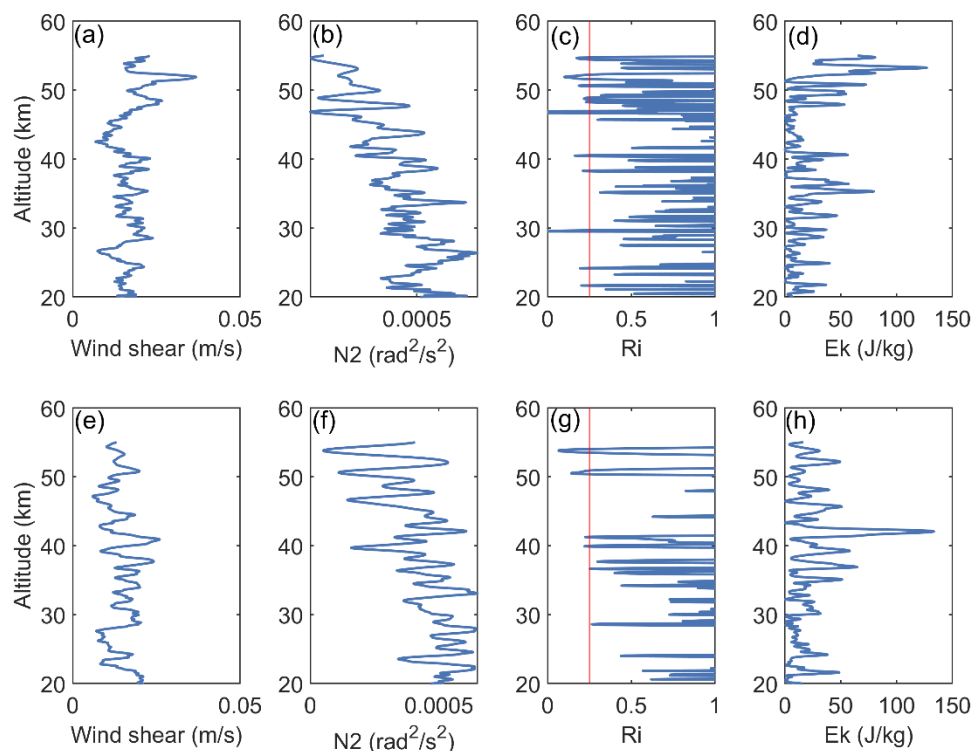
362 Atmospheric GWs can be regarded as superimposed disturbances to the background field. First, a 20-
 363 point sliding average is performed on the profile interpolated with equal spacing (50 m interval) to eliminate
 364 errors caused by random motion and turbulence. Then the smoothing profile is fitted by fifth-order
 365 polynomial to get the background profile. After the background profile is removed, high-pass filtering with
 366 a cut-off wavelength of 10 km is performed to obtain the disturbance profile caused by GWs. The kinetic
 367 energy E_k of GW is calculated by the following formula:

$$368 \quad E_k = \frac{1}{2} (u'^2 + v'^2), \quad (15)$$

369 Where u' and v' are the disturbance components of the zonal and meridional wind field caused by GWs,
 370 respectively.

371 In the error analysis, considering that the error becomes significant above 55 km (Figure 7), the height
 372 interval selected for disturbance analysis here is 20~55 km. The vertical distribution of wind shear, square
 373 buoyancy frequency, Richardson number and kinetic energy obtained according to HJ-1 and HJ-2 detection
 374 results are shown in Figure 9. The wind shear of HJ-1 has the first peak (strongest) near 45-55 km and the
 375 second peak near 30-40 km, while the wind shear peak of HJ-2 is between 30-40 km. The buoyancy frequency
 376 is positive at the whole altitude, indicating that the atmosphere is statically stable, but there is a tendency to
 377 decrease with the increase of altitude. HJ-1 has a buoyancy frequency minimum (even close to 0) between
 378 45 and 55 km, corresponding to large wind shear, resulting in a relatively concentrated area of $R_i < 0.25$,
 379 indicating strong dynamic instability. In contrast, HJ-2 has a smoother profile with smaller wind shear and
 380 larger buoyancy frequency, resulting in fewer dynamic instability regions. For HJ-1, the peak kinetic energy
 381 of GW is above 50 km, corresponding to the maximum value region of wind shear, and the dynamic
 382 instability region is relatively concentrated, indicating that Kelvin-Holtzmann instability has produced strong

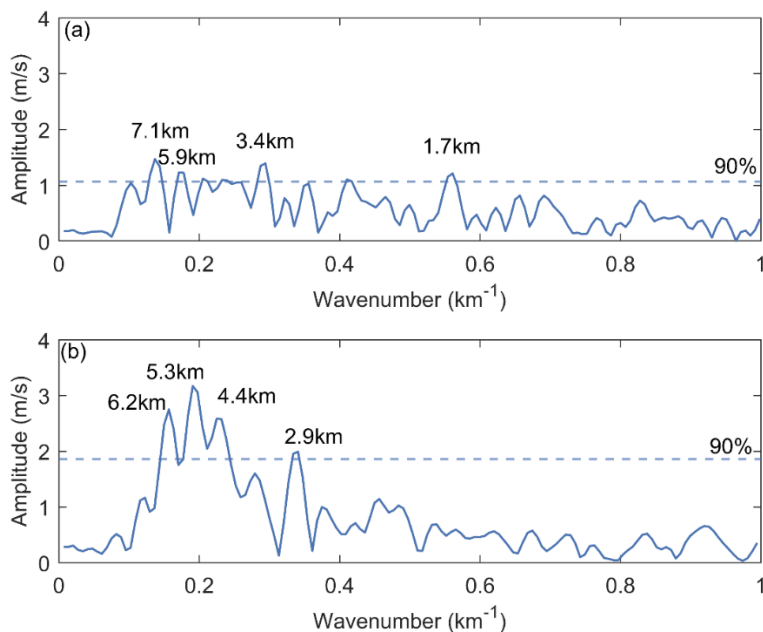
383 high-altitude wave disturbance. Below 50 km, the GW energy of HJ-1 is significantly smaller than that of
 384 HJ-2, which is mainly due to the attenuation of zonal wave disturbance (Figure A5).



385
 386 **Figure 9.** (a) wind shear, (b) square buoyancy frequency, (c) Richardson number and (d) kinetic energy of HJ-1,
 387 and (e) wind shear, (f) square buoyancy frequency, (g) Richardson number and (h) kinetic energy of HJ-2.

388 7.2 Spectral analysis

389 Lomb-Scargle spectrum analysis is performed to the disturbance profile of the synthesized wind speed,
 390 and the vertical wave-number spectrum caused by GWs are obtained, as shown in Figure 10. The amplitudes
 391 of GWs measured by HJ-1 are significantly weaker than those measured by HJ-2, and the vertical
 392 wavelengths of the dominant GWs (amplitudes greater than 90% confidence) are more dispersed, with scales
 393 ranged from 1.7 km to 7.1 km present. In contrast, the dominant GWs measured by HJ-2 have stronger
 394 amplitudes and are concentrated at wavelengths around 4-6 km and 2.9 km.



395
396 **Figure 10. Gravity wave information for (a) HJ-1 and (b) HJ-2 obtained from the disturbance profile of the wind**
397 **field, dashed lines represent 90% confidence, and dominant wavelengths with amplitudes above this threshold are**
398 **labeled.**

399 Through atmospheric instability analysis and GW spectrum analysis, we found that the atmospheric
400 disturbance for HJ-1 is more complex. The GW breaks, resulting in enhanced turbulent activity (more
401 dynamic unstable regions), which also leads to a significant reduction in stratification stability (reduced
402 buoyancy frequency) with more small-scale stratification (Held et al., 2019; van Haren et al., 2015). The GW
403 kinetic energy can be reduced and the amplitude corresponding to the dominant wavelength decreases.
404 Therefore, compared with HJ-2, the measured temperature and wind field profile of HJ-1 have more obvious
405 fluctuations and a denser small-scale layered structure. In addition, the wave energy of HJ-1 is significantly
406 lower than that of HJ-2 in the range of 40-50 km (Figure 9), which is considered to be the main region where
407 wave dissipation occurs. At this time, the zonal and meridional winds of HJ-1 are also smaller than those of
408 HJ-2 between 40-50 km, while their trends and magnitudes below 40 km are indeed similar (Figure 5), which
409 further indicates that wave dissipation weakens the local winds. The fragmentation and dissipation of GWs
410 in the upper stratosphere can reasonably explain the difference of detection profiles in adjacent two days.

411 7.3 Wave dissipation revealed from Stokes parameter method and ERA5 results

412 In order to further prove that the GW at the height of 40-50 km in the detection of HJ-1 has broken up,
413 Stokes parameter method (Vincent et al., 1987; Eckermann., 1996) is used here to extract the typical
414 characteristic parameters of the GW. The main realization path is as follows: Fourier transform is applied to
415 the zonal wind and meridional wind disturbances, and corresponding real and imaginary parts are obtained
416 respectively. Then four Stokes parameters I, D, P and Q are calculated, and information such as scale,

417 propagation and frequency of polychromatic gravity waves can be further obtained. The specific method can
 418 be referred to the previous paper (He et al., 2022).

419 Considering that the wave breaking mainly occurs below 50 km, the GW parameters are calculated for
 420 the two height intervals of 40-50 km and 20-50 km, corresponding to disturbance information in the local
 421 and entire height range, respectively. The kinetic energy, horizontal wavelength, intrinsic frequency, vertical
 422 group velocity and horizontal propagation direction extracted from the two detections are shown in Table 1.
 423 For a local wave disturbance (40-50 km), there is a low-frequency GW of HJ-1, with an intrinsic frequency
 424 (the ratio of wave frequency to inertial frequency) of 2.53. The order of wavelength, kinetic energy and
 425 vertical group velocity is within a reasonable range. In contrast, the intrinsic frequency and vertical group
 426 velocity of HJ-1 are abnormally large, while the horizontal wavelength is abnormally small, which should
 427 belong to the omitted cases. The outliers of the characteristic parameter also reflect the breaking of GWs in
 428 this region from the perspective of abnormal high frequency waves (Fritts and Alexander, 2003), meaning
 429 that GWs can no longer maintain their normal state and dissipate. For the entire wave disturbance (20-50
 430 km), HJ-2 has no obvious wave breaking, and the parameters such as wavelength and frequency are close to
 431 the local disturbance, which means a consistent wave propagation process throughout the entire height. In
 432 contrast, the wavelength and kinetic energy of the entire wave disturbance of HJ-1 are smaller than that of
 433 HJ-2 due to local wave breaking. The wave propagation direction of HJ-2 is significantly different in the
 434 entire and local ranges, possibly due to significant wind speed changes near 40 km (Figure 5c).

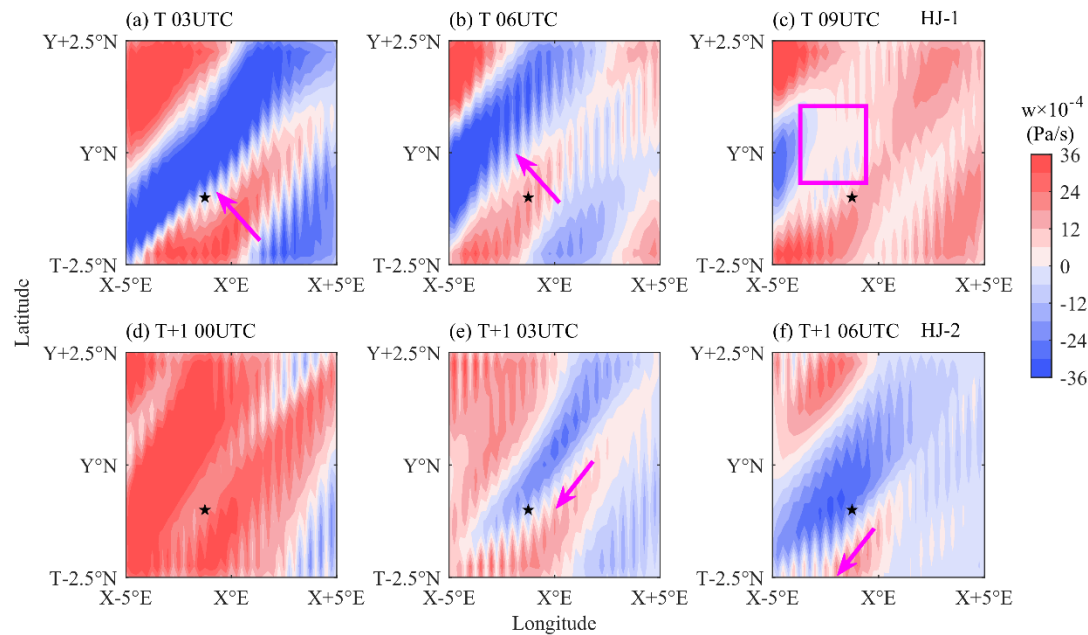
435 Table 1. Gravity wave parameters extracted by Stokes parameter method

detection zone	kinetic energy (J/kg)	horizontal wavelength (km)	intrinsic frequency (w/f)	vertical group velocity (m/s)	horizontal propagation direction
HJ-1 (40-50 km)	13.55	1.08	434.71	15.77	138°
HJ-2 (40-50 km)	28.16	235	2.53	0.088	215°
HJ-1 (20-50 km)	14.38	140	3.74	0.12	145°
HJ-2 (20-50 km)	20.79	296	2.53	0.10	-36°

436 Although the time interval of the two detections is one day apart, considering that the momentum
 437 deposition of GW to the mean flow is continuous and slow (Liu et al., 1999), the comparison of the wind
 438 field results from the two detections may still indicate the effect of GW drag. For the local wave breaking of
 439 HJ-1 (40-50 km), the propagation direction is northwest (the degrees in Table 1 represent angle measured
 440 anticlockwise from x axis), and the deposited momentum produces negative drag (deceleration) on the zonal
 441 wind and positive drag (acceleration) on the meridional wind. Compared with the earlier detection,
 442 significantly stronger meridional wind and significantly weaker zonal wind can be seen near 40 km in the
 443 later detection (Figure 5). This suggests that the drag effect of local wave breaking through deposited
 444 momentum is captured at an altitude of 40 km by HJ-2, and the acceleration of tens of meters per day is also
 445 reasonable (Li et al., 2022).

446 In order to further support the wave breaking at high altitude during HJ-1 detection, ERA5 data is used
 447 to plot the longitude-latitude cross section of vertical velocity at 3hPa (near 41km) in the corresponding

448 region (10° longitude \times 5° latitude), as shown in Figure 12. HJ-1 detection is close to 09UTC (launched at
 449 9.5UTC) on the first day (T), and HJ-2 detection is close to 06UTC (launched at 5.5UTC) on the second day
 450 (T+1). In this pressure layer, the vertical velocity (w) has an obvious alternating positive and negative
 451 perturbation, which indicates the GW activity. For the first day of detection, at 03UTC and 06UTC, the
 452 northwestward movement of the GW is observed. At 09UTC, there is a distinct wave breaking (purple
 453 rectangular box). For the second day of detection, at 03UTC and 06UTC, the southwestward movement of
 454 the perturbation peaks can be observed, and no wave dissipation occurs in the corresponding region. Both
 455 the time of wave dissipation and the direction of wave propagation are consistent with the results calculated
 456 by Stokes parameter method from rocket data (Table 1), which further proves the reliability of the results.



457

458 **Figure 12.** Regional distribution of ERA5 vertical velocity (w) at 3hPa for (a) 03UTC, (b) 06UTC, and (c) 09UTC
 459 on the first day, and (d) 00UTC, (e) 03UTC, and (f) 06UTC on the second day, with the five-pointed star
 460 representing the rocket detection position. The purple arrow represents the direction in which the wave travels,
 461 and the purple rectangular box represents the region where the wave dissipates occurs. The launch point of rocket
 462 is ($X^\circ E, Y^\circ N$).

463 8. Summary

464 In this study, the detection effects and data quality of two meteorological rocket launched in the
 465 northwest of China in the autumn of 2023 are analyzed. First, using the modified temperature correction
 466 model and wind field retrieval algorithm, the atmospheric temperature, pressure, density, wind speed and
 467 wind direction measured by the rocket are obtained, and compared with the matched reanalysis, satellite and
 468 empirical model data. Then, using the methods of error transfer and error synthesis, the measuring error and
 469 data accuracy from rocket detection are calculated, and the influence effect is evaluated. Finally, the
 470 characteristics of atmospheric instability and GW activity are analyzed and discussed. The main conclusions
 471 are as follows:

472 (1) The data acquisition rate of the two rockets is ideal, and the motion trajectory of the ascending and
473 falling stages is normal and smooth. It is a relatively successful detection experiment, which can obtain good
474 quality meteorological data in the range of 20 to 60 km.

475 (2) The rocket detection wind field and MERRA2 wind field have a good agreement below 40 km, and
476 the deviation becomes larger above 40 km. The temperature detection data below 50 km has a good agreement
477 with MERRA2, MISIS and SABER, and the deviation above 50 km begins to increase. The difference in
478 time and space of the matching data, as well as the difference between the model average and the
479 instantaneous detection may be the source of the result bias.

480 (3) Below 50 km, the wind measurement error and temperature measurement error are maintained at a
481 small level, less than 2 m/s and 1.8 °C, respectively. Above 50 km, the error begins to increase. This is
482 because in the early stage of fall, the parachute swing is large, so the position error is large. The data reception
483 is not stable, and the relative speed of the sensor and the air is too large. The above phenomenon leads to the
484 large error.

485 (4) The difference in the intensity of GWs causes the obvious difference in vertical velocity of the
486 dropsonde. For HJ-1, the amplitude of GWs over this region is reduced, and turbulent activity is enhanced,
487 resulting in reduced stability of atmospheric stratification and a denser small scale hierarchical structure on
488 the profile. For HJ-2, the stratification stability of the upper atmosphere is stronger. GWs are more stable and
489 less likely to break, allowing the amplitude to grow to a larger degree.

490 (5) The local breaking of GWs at 40-50 km can be captured ideally from HJ-1. The GWs deposited
491 momentum and energy to the mean flow, and the effect of the wave drag changed the wind field structure
492 below, making HJ-2 with one day delay can detect significant wind field changes near the altitude of 40 km.
493 This reflects the forcing effect of wave dissipation on the background wind field through the observation
494 results. The results of ERA5 data further support the wave dissipation and propagation characteristics
495 extracted by rocket data.

496 The analysis shows that due to the high vertical resolution and in-situ detection method, the rocket drop
497 sounding can capture the fine structure of the atmosphere close to the real state. Accurate and detailed wind
498 field results are very valuable, especially in the region above 30 km. The large measurement error above 55
499 km also indicates that it is necessary to improve the data reception quality at the beginning of the drop, and
500 optimize the high-altitude parachute opening and stability control technology to improve the detection
501 accuracy. The existence of atmospheric gravity wave causes the local feature difference of the detection
502 profile, meaning that the high-altitude disturbance characteristics need to be considered in the rocket
503 detection. This study can support the application of the wave dissipation theory in the upper stratosphere by
504 using the rocket data, while the corresponding ideal observation examples at this altitude are scarce. More
505 subsequent rocket detections are also encouraged to be carried out, thereby improving the cognition level of
506 the near-space atmospheric environment in multi-regions and multi-time.

507

508 **Appendix A**

509

Table A1. Main performance indicators of rocket radiosondes

Indicator name		Performance parameters
Transmitter frequency		400MHz ~ 406MHz
Carrier frequency stability		$\pm 20\text{kHz}$
Emission spectral width		$\leq 50\text{kHz}$ (-50dB)
Transmitter power		100mW ~ 200mW
Digital signal transmission mode		GFSK
Data transmission rate		4800bps
Data update rate		$\geq 2\text{Hz}$
Positioning accuracy	Horizontal direction	5m (CEP 90%)
	Vertical direction	5m (CEP 90%)
	Speed	0.2m/s (CEP 90%)
Temperature	Measurement range	$-90^{\circ}\text{C} \sim +55^{\circ}\text{C}$
	Static calibration accuracy of the sensor	$\leq \pm 0.2^{\circ}\text{C}$
	Resolution	0.1°C
pressure	Measurement range	1060hPa ~ 5hPa
	Static calibration accuracy of the sensor	$\leq \pm 0.8\text{hPa}$
	Resolution	0.1hPa

510

511

512

513

514

515

516

517

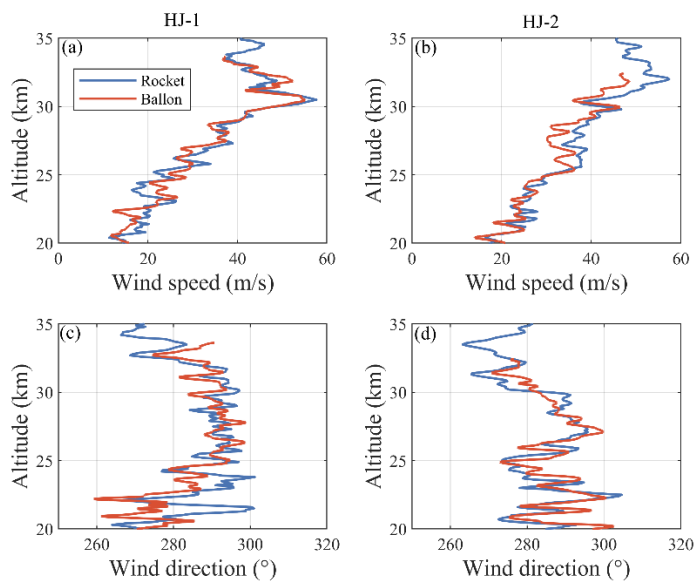
518

Table A2. variable meaning in the equation (6)

variable	meaning	variable	meaning
r	Thermistor boundary layer temperature recovery coefficient	α	Stefan-Boltzmann constant
v_r	The speed at which the thermistor moves with respect to the atmosphere	J	Solar constant
c_p	Specific heat capacity of air at constant pressure	α_t	Absorption rate of long wave by thermistor
$m_T C$	Heat capacity of a thermistor	$A_a/A_b/A_c$	The effective area of the thermistor receiving upper/body/lower bound atmospheric long wave radiation

A	The surface area of the thermistor	$T_a/T_b/T_c$	Equivalent blackbody temperature of upper/body/lower bound atmospheric long-wave radiation source
h	Convective heat exchange coefficient between thermistor and air	ε	Thermistor the emissivity of thermal radiation
$\frac{dT_f}{dt}$	The rate of change of temperature with time	Q_c	Heat conduction coefficient
A_m	The area of the thermistor reflected by the ground and clouds	W_f	Current work coefficient
ρ_m	Combined reflection coefficient of ground and cloud		

519

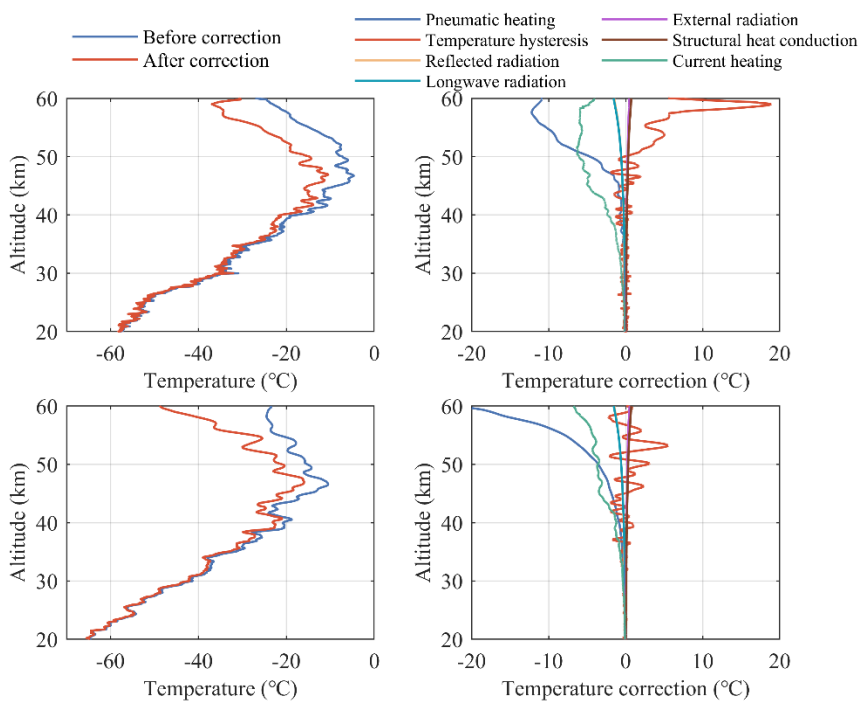


520

521

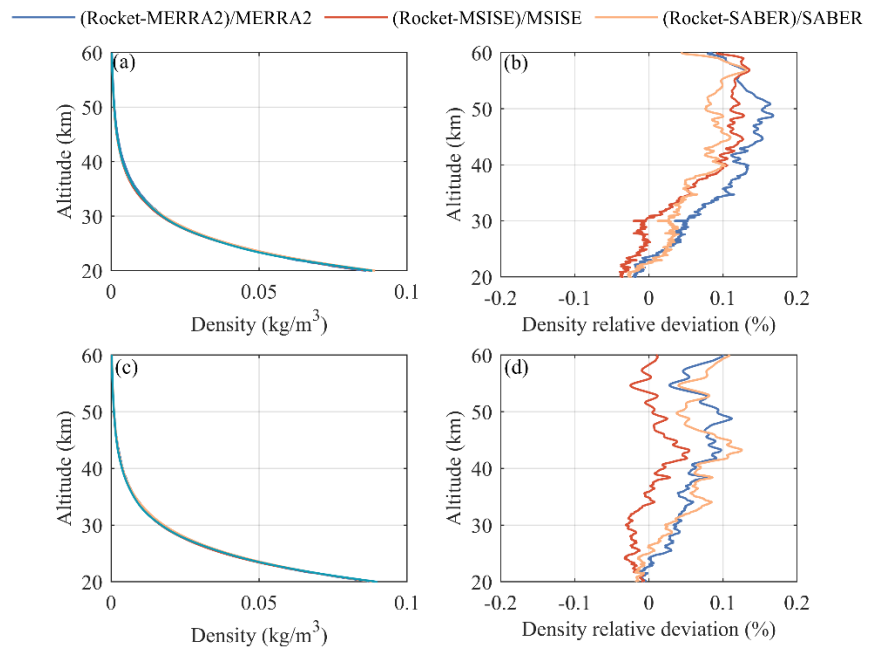
522

Figure A1. Comparison of wind speeds measured by rockets and balloons for (a) HJ-1 and (b) HJ-2, and comparison of wind directions measured by rockets and balloons for (c) HJ-1 and (d) HJ-2



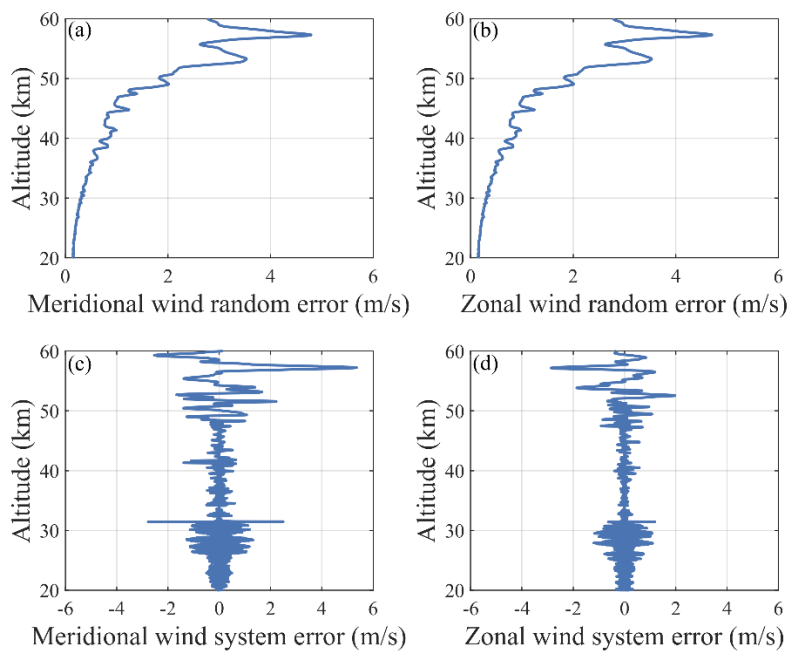
523
524

Figure A2. The vertical distribution of (a) original and corrected temperature, and (b) each correction subterm.



525
526
527
528

Figure A3. The vertical distribution of rocket detection density for (a) HJ-1 and (c) HJ-2. The relative deviation of rocket detection density with MERRA2, MSISE, and SABER for (b) HJ-1 and (d) HJ-2..

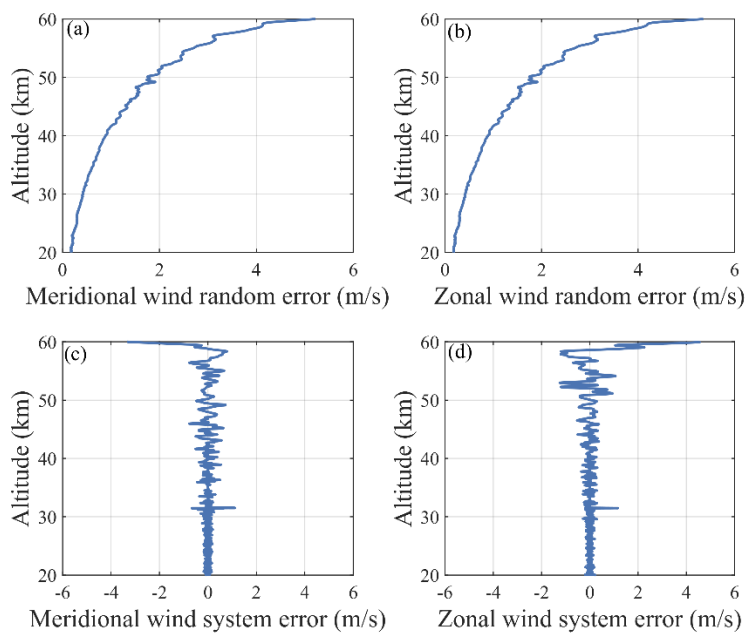


529

530

531

Figure A4. Random error of (a) meridional wind and (b) zonal wind, and systematic error of (c) meridional wind and (d) zonal wind for HJ-1

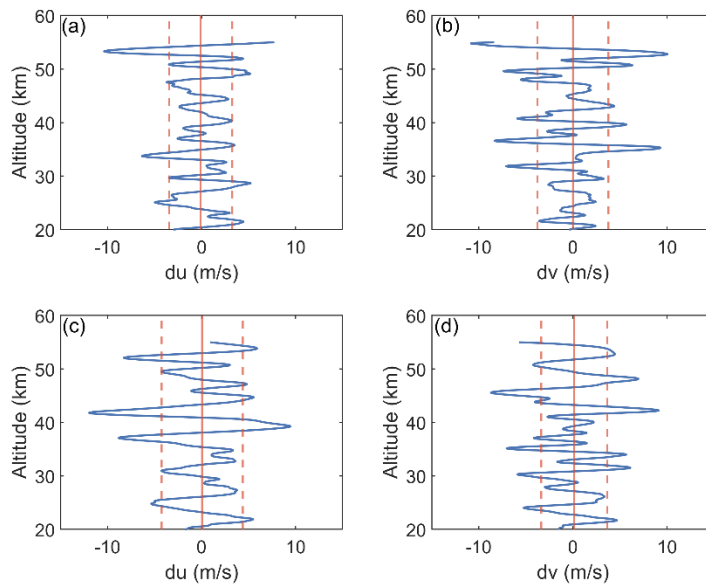


532

533

534

Figure A5. Random error of (a) meridional wind and (b) zonal wind, and systematic error of (c) meridional wind and (d) zonal wind for HJ-2



535

536 **Figure A6. (a) Zonal wind and (b) Meridional wind disturbance profile caused by GWs for HJ-1, and (c) Zonal**
 537 **wind and (d) Meridional wind disturbance profile caused by GWs for HJ-2. The solid and dashed lines represent**
 538 **the mean and standard deviation over the entire height, respectively**

539 Code and data availability

540 SABER data are available from ftp://saber.gats-inc.com/Version2_0/Level2A/ website, MERRA2 data
 541 are available from <https://disc.gsfc.nasa.gov/> website. The data processing scripts and the rocket data are
 542 available from the first author upon reasonable request.

543 Author contributions

544 HM and SZ initiated the study. HY and HJP designed the scheme, HY analyzed data and drew figures,
 545 HY wrote the manuscript. All the authors interpreted results and revised the manuscript.

546 Competing interests

547 The contact author has declared that neither of the authors has any competing interests.

548 Acknowledgments

549 This work was supported by the National Natural Science Foundation of China (Grant no. 42405065)
 550 and the National Natural Science Foundation of China (Grant no. 42275060). Additionally, helpful comments
 551 by the editors and the specific anonymous reviewers are gratefully acknowledged.

552 **References**

- 553 Alexander, M. J., Geller, M., McLandress, C., Polavarapu, S., Preusse, P., Sassi, F., Sato, K., Eckermann,
 554 S., Ern, M., Hertzog, A., Kawatani, Y., Pulido, M., Shaw, T. A., Sigmond, M., Vincent, R., and Watanabe,
 555 S.: Recent developments in gravity-wave effects in climate models and the global distribution of gravity-
 556 wave momentum flux from observations and models, *Q. J. R. Meteorol. Soc.*, 136, 1103–1124,
 557 <https://doi.org/10.1002/qj.637>, 2010.
- 558 Alexander, M. J., Liu, C. C., Bacmeister, J., Bramberger, M., Hertzog, A., and Richter, J. H.: Observational
 559 Validation of Parameterized Gravity Waves From Tropical Convection in the Whole Atmosphere
 560 Community Climate Model, *J. Geophys. Res. Atmos.*, 126, <https://doi.org/10.1029/2020JD033954>, 2021.
- 561 Chen, B., Sheng, Z., and He, Y.: High-Precision and Fast Prediction of Regional Wind Fields in Near
 562 Space Using Neural-Network Approximation of Operators, *Geophys. Res. Lett.*, 50, e2023GL106115,
 563 <https://doi.org/10.1029/2023GL106115>, 2023.
- 564 Daren, L. U., Pan, W., and Wang, Y. B. T.-A. in A. S.: Atmospheric profiling synthetic observation system
 565 in Tibet, *Adv. Atmos. Sci.*, 35, 264–267, 2018.
- 566 Eckermann.: Hodographic analysis of gravity waves: Relationships among Stokes parameters, rotary
 567 spectra and cross-spectral methods, *J. Geophys. Res. Atmos.*, 101, 19169–19174,
 568 <https://doi.org/10.1029/96jd01578>, 1996.
- 569 Eckermann, S. D., Hirota, I., and Hocking, W. K.: Gravity wave and equatorial wave morphology of the
 570 stratosphere derived from long-term rocket soundings, *Q. J. R. Meteorol. Soc.*, 121, 149–186,
 571 <https://doi.org/10.1002/qj.49712152108>, 1995.
- 572 Ern, M., Preusse, P., and Riese, M.: Intermittency of gravity wave potential energies and absolute
 573 momentum fluxes derived from infrared limb sounding satellite observations, *Atmos. Chem. Phys.*, 22,
 574 15093–15133, 2022.
- 575 Fan, Z., Zheng, S., Li, W., Hanqing, S., and Yu, J.: Comprehensive assessment of the accuracy of the data
 576 from near space meteorological rocket sounding, *Acta Phys. Sin.*, 62, 199601, 2013.
- 577 Fritts, D. C. and Alexander, M. J.: Gravity wave dynamics and effects in the middle atmosphere, *Rev.*
 578 *Geophys.*, 41, 1003, <https://doi.org/10.1029/2001RG000106>, 2003.
- 579 Ge, W., Sheng, Z., Zhang, Y., Fan, Z., Cao, Y., and Shi, W.: The study of in situ wind and gravity wave
 580 determination by the first passive falling-sphere experiment in China’s northwest region, *J. Atmos. solar-*
 581 *terrestrial Phys.*, 182, 130–137, 2019.
- 582 Gray, L. J., Anstey, J. A., Kawatani, Y., Lu, H., and Schenzinger, V.: Surface impacts of the Quasi Biennial
 583 Oscillation, *Atmos. Chem. Phys.*, 18, 8227–8247, 2018.
- 584 Guoying, J., Jiyao, X. U., and Dongbo, S.: Observations of the first meteorological rocket of the Meridian
 585 Space Weather Monitoring Project, *Chinese Sci. Bull.*, 56, 2131–2137, 2011.
- 586 van Haren, H., Cimadoribus, A., and Gostiaux, L.: Where large deep-ocean waves break, *Geophys. Res.*
 587 *Lett.*, 42, 2351–2357, <https://doi.org/10.1002/2015GL063329>.Received, 2015.

- 588 He, Y., Zhu, X., Sheng, Z., He, M., and Feng, Y.: Observations of Inertia Gravity Waves in the Western
589 Pacific and Their Characteristic in the 2015/2016 Quasi-Biennial Oscillation Disruption, *J. Geophys. Res.*
590 *Atmos.*, 127, e2022JD037208, <https://doi.org/10.1029/2022JD037208>, 2022.
- 591 He, Y., Zhu, X., Sheng, Z., and He, M.: Identification of stratospheric disturbance information in China
592 based on the round-trip intelligent sounding system, *Atmos. Chem. Phys.*, 24, 3839–3856, 2024.
- 593 Held, P., Bartholomä-Schrottke, K., and Bartholomä, A.: Indications for the transition of Kelvin-Helmholtz
594 instabilities into propagating internal waves in a high turbid estuary and their effect on the stratification
595 stability, *Geo-Marine Lett.*, 39, 139–159, 2019.
- 596 Jin, D., Kim, D., Son, S. W., and Oreopoulos, L.: QBO deepens MJO convection, *Nat. Commun.*, 14, 4088,
597 2023.
- 598 Krivolutsky, A. A., Cherepanova, L. A., and Dement'eva, A. V.: Solar cycle influence on troposphere and
599 middle atmosphere via ozone layer in the presence of planetary waves: Simulation with ARM, *J. Geophys.*
600 *Res. Sp. Phys.*, 120, 8298–8306, 2015.
- 601 Larsen, M. F.: Winds and shears in the mesosphere and lower thermosphere: Results from four decades of
602 chemical release wind measurements, *J. Geophys. Res. Sp. Phys.*, 107, 1215, 2002.
- 603 Larsen, M. F. and Fesen, C. G.: Accuracy issues of the existing thermospheric wind models: can we rely on
604 them in seeking solutions to wind-driven problems?, *Ann. Geophys.*, 27, 2277–2284, 2009.
- 605 Li, T., Ban, C., Fang, X., Li, F., Cen, Y., Lai, D., Sun, C., Sun, L., Zhang, J., and Xu, C.: Seasonal
606 Variation in Gravity Wave Momentum and Heat Fluxes in the Mesopause Region Observed by Sodium
607 Lidar, *J. Geophys. Res. Atmos.*, 127, <https://doi.org/10.1029/2022JD037558>, 2022.
- 608 Lindzen, R. S.: Turbulence and stress owing to gravity wave and tidal breakdown, *J. Geophys. Res.*, 86,
609 9707–9714, <https://doi.org/10.1029/JC086iC10p09707>, 1981.
- 610 Liu, H. L., Hays, P. B., and Roble, R. G.: A Numerical Study of Gravity Wave Breaking and Impacts on
611 Turbulence and Mean State, *J. Atmos. Sci.*, 56, 2152–2177, 1999.
- 612 Organization, W. M.: Guide to meteorological instruments and methods of observation, *WMO Guide To*
613 *Meteorological Instruments And Methods Of Observation*, 2008.
- 614 Qiao, L., Chen, G., Zhang, S., Yao, Q., and Zhang, L.: Wuhan MST radar: Technical features and
615 Validation of wind observations, *Atmos. Meas. Tech.*, 13, 5697–5713, 2020.
- 616 Roney, J. A.: Statistical wind analysis for near-space applications, *J. Atmos. Solar-Terrestrial Phys.*, 69,
617 1485–1501, 2007.
- 618 She, C. Y., Sherman, J., Yuan, T., Williams, B. P., Arnold, K., Kawahara, T. D., Li, T., Xu, L. F., Vance, J.
619 D., and Acott, P.: The first 80-hour continuous lidar campaign for simultaneous observation of mesopause
620 region temperature and wind, *Geophys. Res. Lett.*, 30, 1319, 2003.
- 621 Song, Y., He, Y., and Leng, H.: Analysis of Atmospheric Elements in Near Space Based on
622 Meteorological-Rocket Soundings over the East China Sea, *Remote Sens.*, 16, 402, 2024.
- 623 Thies, B. and Bendix, J.: Satellite based remote sensing of weather and climate: recent achievements and
624 future perspectives, *Meteorol. Appl.*, 18, 262–295, 2011.

- 625 Vincent, Robert, A., Fritts, David, and C.: A Climatology of Gravity Wave Motions in the Mesopause
626 Region at Adelaide, Australia, *J. Atmos. Sci.*, 44, 748–760, 1987.
- 627 Wagner, N. K.: Theoretical time constant and radiation error of a rocketsonde thermistor, *J. Meteorol.*, 18,
628 606–614, 1961.
- 629 Wagner, N. K.: Theoretical Accuracy of a Meteorological Rocketsonde Thermistor, *J. Appl. Meteorol.*, 3,
630 461–469, 1964.
- 631 Wang, L., Fritts, D. C., Williams, B. P., Goldberg, R. A., Schmidlin, F. J., and Blum, A. U.: Gravity waves
632 in the middle atmosphere during the MaCWAVE winter campaign: evidence of mountain wave critical
633 level encounters, *Ann. Geophys.*, 24, 1209–1226, 2006.
- 634 Yoo, J. H., Song, I. S., Chun, H. Y., and Song, B. G.: Inertia-Gravity Waves Revealed in Radiosonde Data
635 at Jang Bogo Station, Antarctica (74°37'S, 164°13'E): 2. Potential Sources and Their Relation to Inertia-
636 Gravity Waves, *J. Geophys. Res. Atmos.*, 125, 1–31, <https://doi.org/10.1029/2019JD032260>, 2020.
- 637 Yuan, Y., Ivchenko, N., Tibert, G., Stanev, M., and Gumbel, J.: Atmosphere Density Measurements Using
638 GPS Data from Rigid Falling Spheres, *Atmos. Meas. Tech. Discuss.*, 12, 1–21, 2017.
- 639
- 640